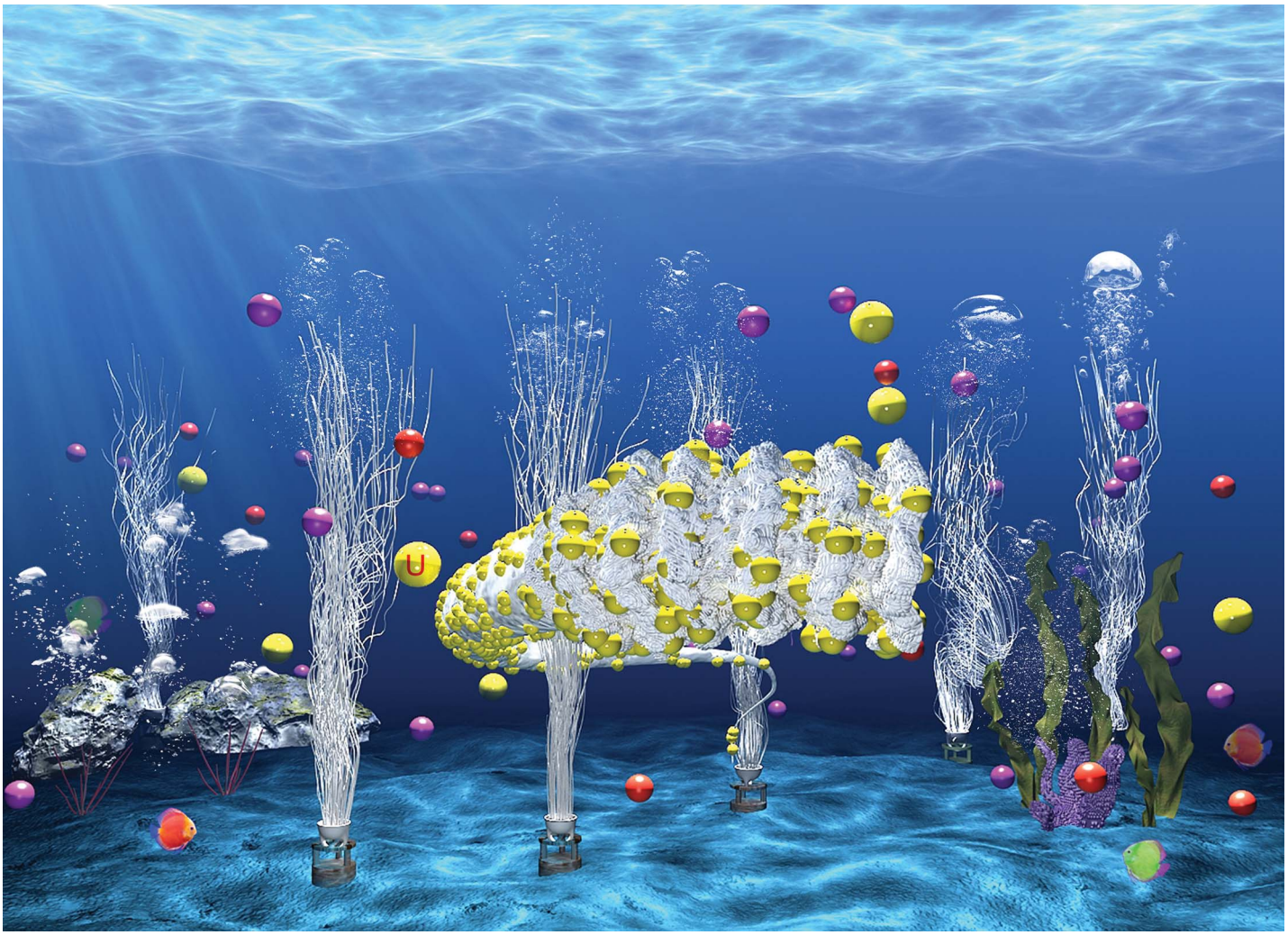

Highlighting research by the group of researchers led by Dr Hongjuan Ma from Shanghai Institute of Applied Physics, Chinese Academy of Sciences, and Dr Shengqian Ma from the University of North Texas.

Ultrahigh and economical uranium extraction from seawater *via* interconnected open-pore architecture poly(amidoxime) fiber

Uranium adsorption performance of AO-OpNpNc fibers is greatly enhanced through an interconnected open-pore architecture poly(amidoxime) fiber with poly(amidoxime) nanoparticles and a nano-channel structure. Easy placement, salvageability, No-extra-drive, low-cost, and ultrahigh uranium capacity AO-OpNpNc fibers are a far more realistic means of massive uranium extraction from seawater, and the exceptional durability of the AO-OpNpNc fibers suggests the possibility of economically producing nuclear fuel from the ocean.

As featured in:

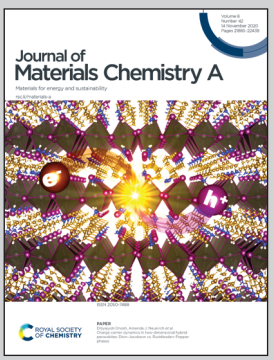

See Shengqian Ma, Hongjuan Ma *et al.*, *J. Mater. Chem. A*, 2020, **8**, 22032.

ROYAL SOCIETY OF CHEMISTRY

rsc.li/materials-a

Registered charity number: 207890

Journal of Materials Chemistry A

ROYAL SOCIETY OF CHEMISTRY

PAPER

View Article Online
View Journal | View Issue

Cite this: J. Mater. Chem. A, 2020, 8, 22032

Ultrahigh and economical uranium extraction from seawater *via* interconnected open-pore architecture poly(amidoxime) fiber†

Xiao Xu, ‡[ab] Lu Xu,‡[b] Junxuan Ao,[b] Yulin Liang,[b] Cheng Li,[b] Yangjie Wang,[b] Chen Huang,[b] Feng Ye,[b] Qingnuan Li,[b] Xiaojing Guo,[c] Jingye Li,[bc] Hengti Wang,[d] Shengqian Ma *[e] and Hongjuan Ma *[b]

Received 22nd July 2020
Accepted 25th August 2020

DOI: 10.1039/d0ta07180c

rsc.li/materials-a

Effectively addressing global warming requires a rapid transformation of the ways in which energy is consumed, and nuclear power produces very low lifecycle carbon emissions. Efficient uranium extraction from unconventional uranium ore sources, such as the ocean, can provide a stable and long-term supply of nuclear fuel for nuclear power plants. Herein, we report an interconnected open-pore architecture poly(amidoxime) (PAO) fiber with PAO nanoparticles and a nano-channel structure (AO-OpNpNc) using a top-down design. A high uranium adsorption capacity of 17.57 mg-U per g-adsorbent in natural seawater and ultra-long service life of at least 30 cycles were obtained, which are the highest values among currently available adsorbents to our knowledge. Extended X-ray absorption fine structure (EXAFS) fits and density functional theory (DFT) computational studies suggest that PAO-bound uranyl is a cooperative chelating model. More importantly, uranium production costs could be reduced to $80.70–86.25 per kg of uranium with this fiber, which is similar to the uranium spot price of $86.68 per kg of uranium and lower than the costs of all currently available adsorbents. The exceptional durability of the AO-OpNpNc fibers suggests the possibility of economically producing nuclear fuel from the ocean.

1. Introduction

Nuclear power production is anticipated to increase with the growing global population. China has the largest nuclear power capacity. The government's long-term target, as outlined in its Energy Development Strategy Action Plan 2014–2020, is to achieve a capacity of 58 GWe by 2020, with the facilities for an additional capacity of 30 GWe under construction.[1] The long-term use of nuclear power for energy applications relies on an economical supply of nuclear fuel.[2] However, according to a recent estimate, one of the main nuclear fuel land-based uranium sources will be depleted by the end of this century.[3] Most of the explored uranium ore in China is of low grade and 90% of the annual uranium fuel relies on imports. Exploration of unconventional uranium resources is a strategic response to the scarcity of uranium resources on land and is critically important to sustain the development of nuclear energy.[4] Fortunately, the oceans hold more than 4.5 billion tons of uranium,[5,6] and uranium extraction from seawater (UES) has a lower environmental impact than terrestrial mining.[7] For this reason, UES has been identified as one of seven chemical separations to change the world.[4]

The challenges of UES are generally due to the extremely low concentration of uranium (3.3 ppb), large amounts of competing ions, and high cost.[8,9] After more than half a century of exploration, it has been proven that adsorption using the amidoxime functional group is the most promising method.[9,10] Multiple adsorbents, including polymeric fibers,[11,12] inorganic materials,[13,14] porous organic polymers (POPs),[15] covalent organic frameworks (COFs),[16–18] and metal–organic frameworks (MOFs),[19–21] have been developed. COFs, POPs, and MOFs with unique porous architectures exhibit good adsorption performances, which are significantly affected by the polymer conformation but not the cyclic imide dioxime or open-chain amidoxime.[22] However, these porous materials are generally in the form of powders or particles, which makes them hard to collect and hampers their practical application.[23] Easy placement, salvageability, low-cost, and high-capacity passive fibrous adsorbent systems are a far more realistic means of massive

[a]Center for Molecular Imaging and Translational Medicine, School of Public Health, Xiamen University, Xiamen 361102, China

[b]Shanghai Institute of Applied Physics, Chinese Academy of Sciences, Shanghai 201800, China. E-mail: mahongjuan@sinap.ac.cn

[c]The Department of Chemistry and Chemical Engineering, Shanghai Normal University, Shanghai 200234, China

[d]College of Materials, Chemistry and Chemical Engineering, Hangzhou Normal University, Hangzhou 310036, China

[e]Department of Chemistry, University of North Texas, 1508 W Mulberry St, Denton, TX 76201, USA. E-mail: Shengqian.Ma@unt.edu

† Electronic supplementary information (ESI) available. See DOI: 10.1039/d0ta07180c

‡ X. Xu and L. Xu contributed equally to this work.

UES.[24] Accordingly, continuous fibrous adsorbent, including a spidroin-based protein fiber (12.33 mg-U per g-adsorbent),[25] a 3D hierarchical porous amidoxime fiber (11.50 mg-U per g-adsorbent),[26] a poly imide dioxime nanofiber (8.7 mg-U per g-adsorbent),[27] and a porous amidoxime-based nanofiber (9.59 mg-U per g-adsorbent),[28] have been developed. The industrialization of UES crucially depends on the properties of the materials, including the adsorption capacity and service life.[26] An estimate for UES adsorbents indicated that an adsorbent with a 30 mg-U per g-adsorbent adsorption capacity, or one with a 6 mg-U per g-adsorbent adsorption capacity at a 3% capacity loss per use for ten uses, would yield $290 per kg-uranium.[29] Despite the availability of these materials and new techniques, their uranium adsorption capacities and economic performances do not meet the disposability requirements of 30 mg-U per g-adsorbent. Accordingly, a supposed 12 mg-U per g-adsorbent adsorption capacity and 30 uses corresponds to a production cost of $75 per kg of uranium,[30] which is comparable to the uranium spot price ($86.68 per kg of uranium, June 26, 2020)[31] and the price of uranium from conventional terrestrial resources.[29]

Traditional fibrous adsorbent encapsulate most of their binding sites in a dense structure, leading to problems of low selectivities and adsorption capacities. Moreover, past studies used fibers as supporting substrates for chemical grafting of the functional groups. Thus, the mass of the trunk fiber adds to the mass of the adsorbent, but provides no adsorption sites. In previous studies, fabricating fibers with hollow gear shapes[32] or porous structures or reducing their diameters to the nanoscale[27] could increase the specific surface areas of the adsorbents, but this inevitably decreased their mechanical strengths. The high specific surface area of adsorbents and the high utilization efficiency of functional groups stand for high adsorption capacities, ultrahigh mechanical strengths, and stable chemical structures to ensure the long service lives of the adsorbents. The balance of these two key factors has haunted researchers for years. Thus, endowing a high specific surface area and high utilization efficiency of functional groups to a continuous fibrous adsorbent with an ultrahigh mechanical strength is highly desired.

The combination of radiation-induced co-grafting polymerization (RIGP) and Ce^{4+}-initiated co-grafting polymerization (CIGP) enabled the tuning of the morphologies of the fibers, which was confirmed in our previous study using PE-coated polypropylene (PP) skin-core fibers.[26] The tunable morphologies of the obtained H-ABP fibers contained uniform PAO particles on the grafted PE skin layer, which showed an average polymeric particle size of about 500 nm. The mechanical properties of these H-ABP fibers were supported by the PP core layer. However, the unmodified PP core layer provided no active sites for adsorption, which limited the adsorption capacity of the material. In this work, we report interconnected open-pore architecture ultra-high molecular weight polyethylene (UHMWPE) fibers with poly(amidoxime) (PAO) nanoparticles and nano-channel structures (AO-OpNpNc) using a top-down design (Fig. 1a–c). The adsorbent design was inspired by the reverse protocols for COFs, whose porous architectures are fabricated from monomers. The bottom-up design of COFs reveals that functional groups with porous architectures result in good properties. In contrast, a top-down design using macromolecules in the form of a continuous fibrous material should open a new approach for adsorbent synthesis. AO-OpNpNc fibers were fabricated *via* a facile method of two-step co-grafting polymerization involving the RIGP followed by the CIGP. Self-assembly from the grafted chains resulted in a nanostructure, and the use of trunk UHMWPE fibers resulted in self-supporting interconnected open-pore architecture fibers, which maximized the functionality of the substrate materials. These two innovations yielded a breakthrough in the material properties. UHMWPE fibers, which were the only candidates for fabricating self-assembling and self-supporting interconnected open-pore architecture fibers, were used as the trunk fibers. To the best of our knowledge, the new morphologies of the open-pore structure with the PAO nanoparticles and nano-channels of the UHMWPE fiber are the first reported. Extended X-ray absorption fine structure (EXAFS) analysis and density function theory (DFT) calculations revealed that the uranyl binding occurred through a chelating mode. The well-designed morphological structure of the AO-OpNpNc fibers maximized the fiber specific surface areas and improved the utilization efficiency of the amidoxime groups, leading to the best uranium adsorption capacity, strongest mechanical strength, and longest service life for UES reported to date. The uranium production cost (UPC) was greatly reduced, which not only meets the economic criteria for UES adsorbents but also is highly competitive with traditional uranium mining.

2. Experimental section

2.1 Chemicals and materials

Ultrahigh molecular weight polyethylene (UHMWPE) fiber (TYZ Safetex FT-103) was purchased from Beijing Tongyizhong Advanced Material Company. 2-Hydroxyethyl acrylate (HEA), copper(II) sulfate pentahydrate ($CuSO_4 \cdot 5H_2O$), acrylonitrile (AN), acrylic acid (AA), ceric ammonium nitrate (CAN), nitric acid (HNO_3), *N*,*N*-dimethylformamide (DMF), sodium carbonate (Na_2CO_3), potassium hydroxide (KOH), hydrochloric acid (HCl), nitric acid (HNO_3), hydroxylamine hydrochloride ($NH_2OH \cdot HCl$) and methanol were purchased from Sinopharm Chemical Reagent Company. All chemicals from commercial sources were of reagent grade and used without further purification. Nitrogen gas (99.99% purity) was obtained from Shanghai Louyang Gas Canned Co., Ltd. Baysalt was obtained from the salt fields in Qingdao, Shandong Province, China, and used without any refining. The 1000 ppm standard solutions of uranium and competing ions were purchased from SPEX Certi Prep, Inc. High-purity deionized water (PALL, Cascada BIO) was used for all experiments unless otherwise stated.

2.2 Synthesis of AO-OpNpNc fiber

UHMWPE fibers were used as the trunk material for the preparation of the AO-OpNpNc fibers. The UHMWPE fiber was pre-irradiated with an electron beam (EB) in air at room temperature with an absorbed dose range from 20 to 100 kGy. After

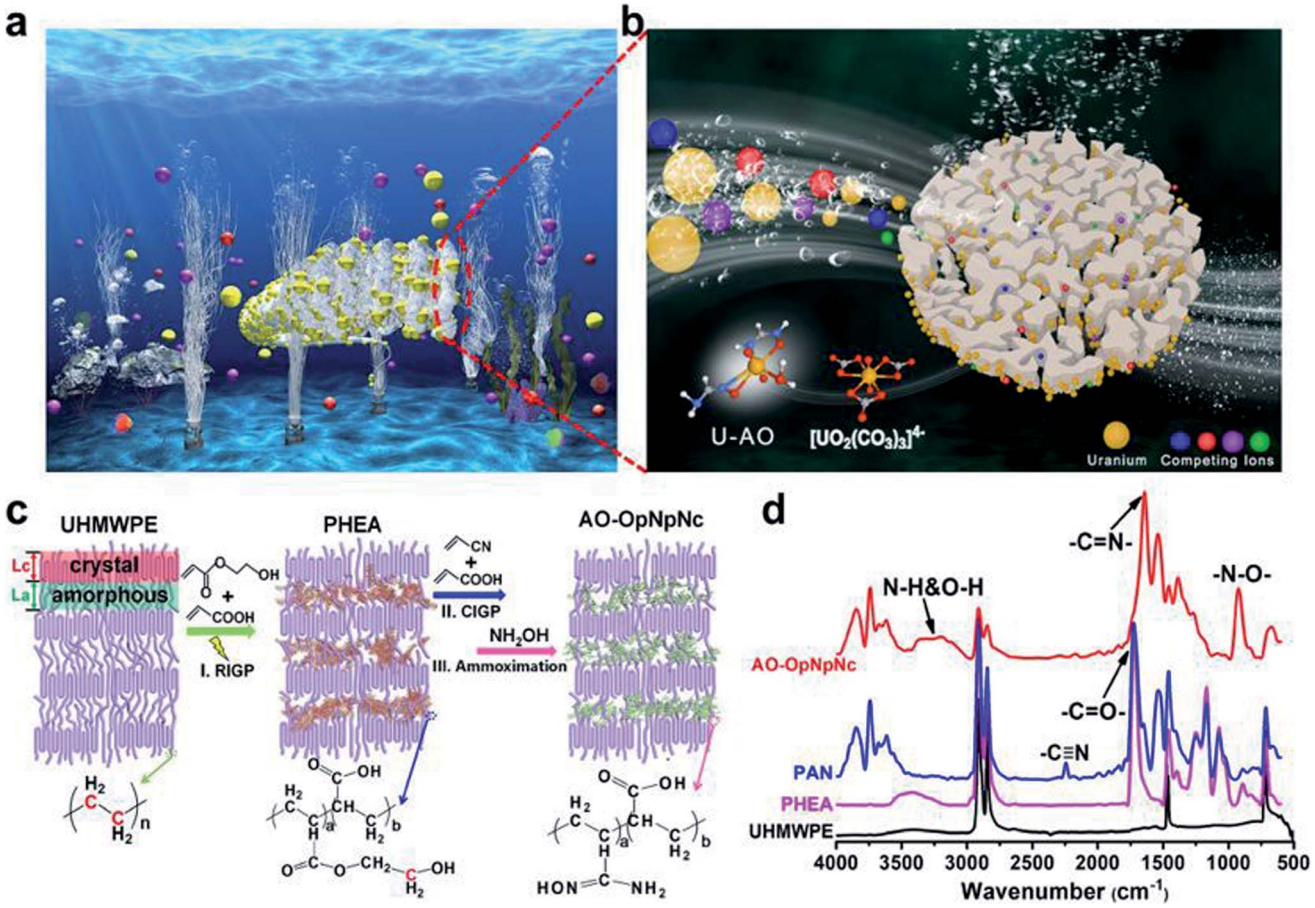

Fig. 1 Strategy for developing an interconnected open-pore architecture adsorbent with PAO nanoparticles and a nano-channel structure. (a) Conceptual drawing: easy placement, salvageability, low-cost, and ultrahigh uranium capacity AO-OpNpNc fibers are a far more realistic means of massive UES. (b) Mechanism of uranyl chelation with the amidoxime groups in the nano-channel structure of the AO-OpNpNc fibers. The interconnected open-pore architectures of the AO-OpNpNc fibers provided numerous nano-channels for continuous mass transport, leading to an ultrahigh uranium adsorption capacity. (c) Schematic diagram of the preparation of AO-OpNpNc fibers: co-grafting and ammoximation in the amorphous UHMWPE fiber. (d) FT-IR spectra of UHMWPE, PHEA, PAN, and AO-OpNpNc fibers.

irradiation, the pre-irradiated UHMWPE fiber was placed in a flask containing a monomer solution and then purged with nitrogen gas for 15 min to remove the oxygen. The monomer solution was prepared with 20 vol% HEA and 20 vol% AA in an aqueous solution. Co-graft polymerization was performed in a water bath for 5 h at 60 °C. Subsequently, the poly-HEA-*co*-AA (PHEA) fiber was washed with H_2O to remove homopolymer and residual monomers and dried in a vacuum oven at 60 °C. The degree of grafting (DG) of the PHEA fiber was calculated as follows:

$$\mathrm{DG}(\%) = \frac{M_1 - M_0}{M_0} \times 100 \quad (1)$$

where M_0 is the weight of the original UHMWPE fiber, and M_1 is the weight of the PHEA fiber.

Subsequently, PHEA fiber with a DG of 28.5% was immersed in a flask containing a monomer solution of AN/AA/DMF (32 vol%/8 vol%/60 vol%). After purging with nitrogen gas for 15 min, 5 mL of Ce^{4+} solution (0.1 mol L^{-1} ceric ammonium nitrate in 1 mol L^{-1} HNO_3) was added to the monomer solution immediately. The co-grafting polymerization was performed in a water bath for 0.5–6 h at 35–65 °C. After co-grafting, the poly-AA and poly-AN (PAN) fibers were washed with DMF to remove residual monomers and homopolymers and dried in a vacuum oven at 60 °C. The DG of the PAN fiber was calculated as follows:

$$\mathrm{DG}(\%) = \frac{M_2 - M_1}{M_1} \times 100 \quad (2)$$

where M_1 is the weight of the PHEA fiber, and M_2 is the weight of the PAN fiber.

Next, a 10 wt% solution of $NH_2OH \cdot HCl$ was prepared using a bicomponent solvent composed of H_2O (50 vol%) and methanol (50 vol%). The pH of the solution was adjusted to neutral with KOH. PAN fibers were placed into the $NH_2OH \cdot HCl$ solution at 70 °C for 24 h to convert the nitrile groups into AO groups. After amidoximation, the obtained AO-OpNpNc fibers were washed with deionized water to remove the unreacted NH_2OH and then dried in a vacuum oven at 60 °C. The AO group density of the AO-OpNpNc fiber was determined using the following equation:

$$\text{AO density}\left(\text{mmol g}^{-1}\right) = \frac{1000 \times (M_3 - M_2)}{33 M_3} \times 100 \qquad (3)$$

where M_2 and M_3 are the weights of PAN and AO-OpNpNc fiber, respectively, and 33 is the molecular weight of the AO group minus the molecular weight of the nitrile group.

2.3 Characterization techniques

Fourier-transform infrared (FT-IR) spectra were collected on a Nicolet Avatar 370 FTIR spectrometer (Thermo Nicolet Company, USA) in attenuated total reflectance mode with a resolution of 4 cm^{-1} and 32 scans. The elemental composition and chemical states of the fibers were analyzed by X-ray photoelectron spectroscopy (XPS) using a Thermo SCIENTIFIC ESCALAB 250Xi instrument. The XPS data were acquired through wide scans ranging from 0 to 1300 eV.

Nitrogen adsorption–desorption isotherms were measured by a surface aperture adsorption instrument (ASAP2010C, Micromeritics, USA). The specific surface areas of the samples were calculated using Brunauer–Emmett–Teller (BET) method within a relative pressure (P/P_0) range of 0.0–1.0, and the pore size distribution were calculated by the Barret–Joyner–Halenda (BJH) algorithm.

The fiber samples were embedded in epoxy resin and ultra-microtomed at −140 °C to a section with a thickness of about 70 nm, where the phase structure of the fiber cross-section was examined and multiple energy dispersive X-ray spectroscopy (EDX) was performed using transmission electron microscopy (TEM, Jeol 2010) at an accelerating voltage of 200 kV.

The surface and cross-sectional morphologies of the fiber samples and the energy dispersive spectroscopy (EDS) analysis was performed using field-emission scanning electron microscopy (SEM) (JSM-6700F, JEOL, Japan). All the fibers were frozen and cracked in liquid nitrogen to investigate the original cross-section morphologies. All the fiber samples were sputtered with gold to enhance the electron conductivity before observation by SEM.

Wide-angle X-ray diffraction (WAXD) measurements were carried out on an X'Pert Pro MPD instrument (Netherlands), with 2θ values from 10 to 90° at room temperature. The full width at half maximum (FWHM) was quantitatively analyzed through Gaussian multipeak fitting and plotted.

Differential scanning calorimetry (DSC) measurements were performed on a NETZSCH STA449F3-QMS instrument (Germany) from 30 to 200 °C at a heating rate of 5 °C min^{-1} and a nitrogen gas flow rate of 20 mL min^{-1}. The crystallinity (X_c) was calculated from the enthalpy (ΔH_m) of the crystallite and the heat of fusion of the 100% crystalline material (ΔH_0 291 J g^{-1}).[33,34]

Mechanical tests were conducted on a universal material testing machine (TIDJ-1000, Suzhou Zhuo Xu Precision Industry Co. Ltd., China).

TGA was performed (NETZSCH, TG209, F3) in the temperature range from 25 to 800 °C with a heating rate of 10 °C per minute under a nitrogen flow.

The concentrations of the metal ions in the simulated and natural seawater were determined by ICP-AES (PerkinElmer Optima 8000). The average of three replicate measurements per sample was used to quantify the uranium and other coexisting ions against a four-point calibration curve. ICP-MS (Perkin Elmer, NexION 300D) was used for quantitative analysis.

Extended X-ray absorption fine structure (EXAFS) spectra of $UO_2(NO_3)_2 \cdot 6H_2O$ solid samples and U-AO-OpNpNc fibers were collected at the uranium L_{III}-edge (17 166 eV) using a double crystal monochromator (Si 111) in a transmission mode at room temperature on Beamline BL14W1 of Shanghai Synchrotron Radiation Facility (SSRF). Energy calibration was performed using a zirconium foil (17 998 eV) as the reference for energy calibration and measured simultaneously for all samples. Each sample was measured thrice. The electron beam energy of the storage ring was 3.5 GeV, and the maximum stored current was approximately 210 mA. Data for $UO_2(NO_3)_2 \cdot 6H_2O$ solid standards were collected in transmission mode, while data for uranium-exposed AO-OpNpNc fibers were collected in the fluorescence geometry. The self-absorption effects were corrected prior to analysis. The EXAFS spectra analysis was performed with Athena and Artemis packages[35] based on the IFEFFIT program.[36] In the Fourier transform k^3-weighted XAFS functions, the k range of 2.8–13.6 Å was used, and the fitting was performed in the R-space (1.0–3.7 Å) using FEFFIT. The theoretical backscattering phase and amplitude functions for the fitting were calculated using the FEFF 8.2 code.[37]

2.4 DFT calculation method

To save computational efficiency, a unit of AO-OpNpNc was chosen as a computational model. Density-functional calculations were implemented in the Gaussian 09 program[38] using the B3LYP level of theory,[39,40] which has been widely utilized and proven to be sufficiently accurate for extensive systems. The quasi-relativistic effective core potentials (RECP) replacing 60 core electrons for actinides and the corresponding valence basis sets were used for uranium,[41,42] and the valence electrons in this basis set are represented by a contracted [8s/7p/6d/4f] basis; 6-311G(d,p) basis set was used for H, C, N, and O atoms. In previous studies confirmed that this level of theory can get accurate geometries and energetics for actinide species.[43] It is worth nothing that the reliability of the computational setup has been also justified that the structural properties after optimization agree well with experiments. Frequency calculations were performed to verify that geometries were minima. Binding enthalpies were calculated as follows:

$$\Delta H = E(\text{complex}) - E(\text{donor}) - E(\text{acceptor}) + \Delta E_{\text{ZPE}} + \Delta E_{\text{thermal}} + \Delta(PV),$$

where Δ represents difference between complex and free species and $\Delta(PV) = RT = -0.593$ kcal mol^{-1} at 298.15 K.[40] The influence of aqueous solvation was modeled by performing single-point calculations on previously optimized geometries with the Integral Equation Formalism for Polarized Continuum Model (IEF-PCM).[40]

2.5 Simulated seawater screening and reusability of AO-OpNpNc fiber

Batch adsorption and 30 adsorption–desorption cycles were performed using 5 L plastic tanks of simulated seawater. First,

175 g sea salt was dissolved in 5 L deionized water to produce a salinity of 35 practical salinity units (psu). Next, a certain amount of uranium and competing ion standard solutions were added into the 5 L solution. The initial concentrations of the uranium and competing metal ions VO^{3-}, Fe^{3+}, Co^{2+}, Ni^{2+}, Cu^{2+}, Zn^{2+}, and Pb^{2+} in the simulated seawater system were about 100 times higher than that in natural seawater. The pH value was adjusted to 8.0 ± 0.1 with 0.25 g of Na_2CO_3. Before adsorption the AO-OpNpNc fiber was conditioned by adding 0.1 g to a flask containing 30 mL of 2.5% KOH at 60 °C for 1 h and was washed with deionized water until the pH of the excess water in the AO-OpNpNc fiber was neutral. Next, approximately 0.1 g of the AO-OpNpNc fibers was added to 5 L of simulated seawater. The adsorption experiment was carried out on a rotary shaker at 25 °C and 100 rpm for 24 h. The uranium and competing metal ions loaded onto the AO-OpNpNc fibers were eluted with 0.1 M HCl solution at room temperature with a rotary shaker at 100 rpm for 30 min. The concentration of the eluted uranium was analyzed by inductively coupled plasma atomic emission spectroscopy (ICP-AES) with an appropriate dilution. The adsorption capacity of the AO-OpNpNc fibers for metal ions could be determined using eqn (4):

$$Q = CV/M, \tag{4}$$

where Q (mg g^{-1}) is the adsorption capacity of the metal ions from AO-OpNpNc fibers, C (mg L^{-1}) is the metal ion concentration measured by ICP-AES or inductively coupled plasma mass spectroscopy (ICP-MS), V (L) is the eluted solution volume, and M (g) is the weight of the dried AO-OpNpNc fiber that was used. After elution, the AO-OpNpNc fibers were immersed in 0.1 M NaOH solution at room temperature for 20 min for regeneration, and then was rinsed with deionized water until the pH of the excess water in the AO-OpNpNc fiber was neutral. The adsorbent was used for the next adsorption–desorption cycle following the same procedure as that described in this section above.

2.6 Uranium adsorption in natural seawater

Natural seawater from the coastal area of Raoping, Guangdong Province, China (117.08° E, 23.58° N) was used for adsorption tests. Batch adsorption was performed first using the same adsorption test protocol carried out in the Oak Ridge National Laboratory, USA.[44] 5 mg of AO-OpNpNc fiber was added to 20 L of natural seawater and the container was shaken constantly at 100 rpm at room temperature, and samples were periodically collected using a pipette over a period of about 50 d. Once the concentration of uranium in the seawater was constant, the adsorbent was taken out and put in another container with 20 L of fresh seawater to repeat the adsorption process. In total, 60 L of natural seawater was used, and the adsorption process lasted for about three months. ICP-MS was used for quantitative analysis. Seawater standards of CASS-6 (seawater), supplied by the National Research Council of Canada, were used for seawater quality-control experiments. High-purity nitric acid (2%) was used as the sample diluent and carrier phase. The uranium adsorption capacity of the AO-OpNpNc fiber could be determined using eqn (5):

$$Q = (C_0 - C_t)V/M, \tag{5}$$

where Q (mg g^{-1}) is the uranium adsorption capacity of the fibers, C_0 and C_t (mg L^{-1}) are the concentration of uranium before and after adsorption, respectively, V (L) is the seawater volume, and M (mg) is the weight of the dried AO-OpNpNc fiber before adsorption.

After adsorption, the AO-OpNpNc fibers were removed and eluted with 0.1 M HCl. High-purity deionized water was then added to produce a dilute acid solution and obtain a desired uranium concentration range for analysis. The amounts of uranium and other co-existing ions were calculated using the following equation:

$$Q = CV_d/M, \tag{6}$$

where Q (mg g^{-1}) is the adsorption capacity of the fibers for each metal ion, C (mg L^{-1}) is the concentration of the metal ions measured by ICP-AES, V_d (L) is the elution solution volume, and M (g) is the weight of the dried AO-OpNpNc fibers after adsorption.

The marine adsorption test was performed in the coastal area of Raoping, Guangdong Province, China. The natural seawater adsorption test in this study was carried out at an average uranium concentration of 3.1 ± 0.3 ppb, an average pH of 8.0 ± 0.1, salinity of 29.6 ± 0.4 psu, temperature of 26.4 ± 0.4 °C. The natural seawater was pumped to an underground impounded reservoir. After filtering out the sediment with a polyester non-woven fabric, the seawater was pumped into a flume. The flow rate of the flume could be controlled with a motor controller. The inlet flow rate was adjusted to 1.5 L min^{-1}, the flume size was 152.6 × 8 × 15 cm and the flow velocity was 0.2 cm s^{-1}.[26] The AO-OpNpNc fibers after KOH treatment was immersed in the flume. The duration of the marine test was 90 days. Three independent samples were collected and rinsed with deionized water three times and then dried in a vacuum oven at 60 °C for 24 h. The AO-OpNpNc fibers were digested in 10 mL of high-purity concentrated nitric acid at a programmed temperature (25 min of heating from 25 to 190 °C, holding for 25 min, followed by natural cooling) using a MARS6 Microwave Digestion System (CEM, USA). High-purity deionized water was then added to produce a dilute acid solution and obtain a desired uranium concentration range for analysis. The amounts of uranium and other co-existing ions were calculated using the eqn (6).

2.7 Uranium extraction from the ocean

The AO-OpNpNc fibers were prepared in a 10 L reaction kettle with a liquor ratio of 1 : 20 (500 g of trunk UHMWPE fiber with 10 L monomer solution). The other experimental parameters were same as those for the synthesis of the AO-OpNpNc fibers in the first part of the ESI.† The DG of the PHEA fiber was calculated to be 20.8%, and that of the PAN fibers was calculated to be 95.0%. The AO group density of the AO-OpNpNc fibers was

calculated to be 5.03 mmol g^{-1}. Approximately 1 kg of AO-OpNpNc fiber was prepared. After KOH conditioning and washing with tap water, the fibers were placed into a 2 m^3 vat with cable ties at Tropical Marine Biological Research Station in Hainan, South China Sea Institute of Oceanology, Chinese Academy of Sciences, Sanya, Hainan, China. Seawater was pumped into the vat with a flow velocity of 100 L min^{-1}, and fresh seawater was fed into the system every 30 min. After 3 months of adsorption, the adsorbents were removed and washed with tap water to remove contaminants. The adsorbents were then spin-dried and eluted with 25 L 0.1 M HCl overnight. The eluant was concentrated to 5 L using reduced pressure distillation, and the precipitated phase was removed from the solution. The solution was then concentrated to 1 L. Ammonia was slowly added into the solution until no more precipitate appeared. Yellowish-brown precipitates in the solution were obtained by suction filtration and were dried in a vacuum oven at 60 °C. Finally, 32.02 g of crude uranium was obtained, and the uranium concentration in the compound was determined to be 17.5% with ICP-AES.

3. Result

3.1 Synthesis and structural analysis of AO-OpNpNc fibers

Continuous fibrous adsorbents are considered to be the materials with the greatest potential in the field of UES, as they are easily placed and recovered and require no extra power for uranium extraction (Fig. 1a). The primary challenge in material design in the field of UES is how to obtain a balance between high adsorption capacity and strong mechanical strength. UHMWPE fibers with high molecular weights, high crystallinities, and high strengths are the most suitable candidate for UES.[45] However, because of their excellent chemical corrosion resistance, modification of UHMWPE with traditional methods is hypodynamic. Herein, AO-OpNpNc fibers were synthesized *via* two-step co-grafting polymerization (Fig. 1c).[26] The RIGP of 2-hydroxyethyl acrylate (HEA) and acrylic acid (AA) occurred in the amorphous region of UHMWPE to provide hydroxyl groups (–OH) as reducing agents in the obtained PHEA fiber. The subsequent CIGP of acrylonitrile (AN) and AA on specific sites of the poly-HEA side chains using Ce^{4+} as a strong oxidant yielded axial grafting chains, which resulted in poly-AN-*co*-AA (PAN) fibers with interconnected open pores architectures, PAN nanoparticles, and nano-channels *via* self-assembly. The mechanism of CIGP was reported in our previous publication.[26] Finally, amidoximation of the PAN fibers resulted in AO-OpNpNc fibers. The RIGP and CIGP were systematically studied to investigate the optimal grafting conditions (Fig. S1, ESI†). The degree of grafting (DG) of the PHEA fibers increased linearly with increasing absorbed dose and reached 28.5% at 40 kGy. CIGP, which was carried out with 40% AN and AA (4/1 wt/wt) in DMF at 55 °C for 2 h yielded PAN fibers with 188.6% DG of poly-AN-*co*-AA. After amidoximation, the amidoxime group density of the obtained AO-OpNcNp fiber was 6.8 mmol g^{-1} (eqn (3)). The successful preparation of the AO-OpNpNc fibers was determined *via* FT-IR (Fig. 1d) and XPS (Fig. S2, ESI†). After RIGP, the new characteristic adsorption bands at 1722 and 1074.3 cm^{-1} were attributed to the adsorption of –C=O– and –C–O–, respectively. After CIGP, the PAN fibers showed new stretching vibrations of –C≡N at 2247 cm^{-1}, indicating that HEA, AA, and AN were successfully grafted onto the trunk UHMWPE fibers. After amidoximation, the disappearance of the nitrile stretching at 2247 cm^{-1} and the appearance of $–NH_2$/–OH (3140–3450 cm^{-1}), –C=N– (1643 cm^{-1}), C–N (1381 cm^{-1}), and N–O (920 cm^{-1}) confirmed the conversion of nitrile groups to amidoxime groups.[11,26] In the XPS spectra (Fig. S2a, ESI†), compared with the trunk UHMWPE fibers, the PHEA fibers showed a new peak at 532.0 eV (O 1s), indicating the successful co-grafting of PHEA and PAA on the trunk UHMWPE fibers. Following co-grafting and chemical modification, the N 1s (399.2 eV) peak appeared for the PAN and AO-OpNcNp fibers, suggesting that a successful reaction between PAN and NH_2OH occurred. The high-resolution C 1s spectrum of the AO-OpNpNc fibers was curve-fit with four peak components, which were attributed to C–C (284.6 eV), C–O (286.0 eV), C=N (286.5 eV), and O–C=O (288.5 eV) (Fig. S2b, ESI†). Furthermore, the high-resolution O 1 s spectrum of the AO-OpNpNc fibers, as shown in Fig. S2c (ESI),† contained three peaks, which were attributed to C=O (531.5 eV), N–O (532.0 eV), and C–O (533.0 eV). The high-resolution N 1 s spectrum containing $C–NH_2$ (399.5 eV) and C=N–OH (400.5 eV) peaks (Fig. S2d, ESI†) further illustrated that the AO-OpNpNc fibers were successfully synthesized.

Scanning electron microscope (SEM) images of the surface morphologies of the fibers and transmission electron microscope (TEM) images of the cross-sectional morphologies are shown in Fig. 2. The trunk UHMWPE had an average diameter of 20.2 ± 0.3 μm and exhibited smooth surfaces, with compact interior regions (Fig. 2a, e, and S3a, ESI†). Because of the relatively low DG of 28.5% after the RIGP of the HEA and AA, the diameters and the surfaces of the PHEA fibers showed no significant changes (Fig. 2b and S3b, ESI†). The following CIGP of AN and AA resulted in a significant diameter increase to 52 ± 3 μm (Fig. 2c). Nanoparticles with an average diameter of 276.4 ± 0.6 nm were obtained, and gaps between the nanoparticles with an average diameter of 60 ± 5 nm were obtained on the surfaces of the PAN fibers (Fig. 2c and g). In the view range of ~30 μm of the cross-sections, the interior regions of the PAN fiber exhibited open pores with nanoparticles and nano-channels (Fig. 2g and S3c, ESI†). The statistical distribution of the internal particles from the cross-section of the PAN fibers revealed diameters in the range of 210–330 nm; an average diameter of 276.4 nm was obtained by ImageJ software analysis (Fig. S4, ESI†). Furthermore, energy dispersion spectroscopy (EDS) and multiple EDX mappings of N in the PAN fiber cross-sections indicated that –C≡N was distributed throughout the nanoparticles (Fig. S3c and S4, ESI†). The interconnected open-pore architecture, PAO nanoparticles, and nano-channel structure in the AO-OpNpNc fibers can be easily discerned from the SEM and the TEM images (Fig. 2d and h). After ammoximation, the morphologies of the AO-OpNpNc fibers remained on the surfaces and inside the fibers. PAO nanoparticles (270 ± 2 nm) on the surface and inside became smaller, and the internal gaps (80 ± 4 nm) grew slightly compared with those of the PAN fibers.

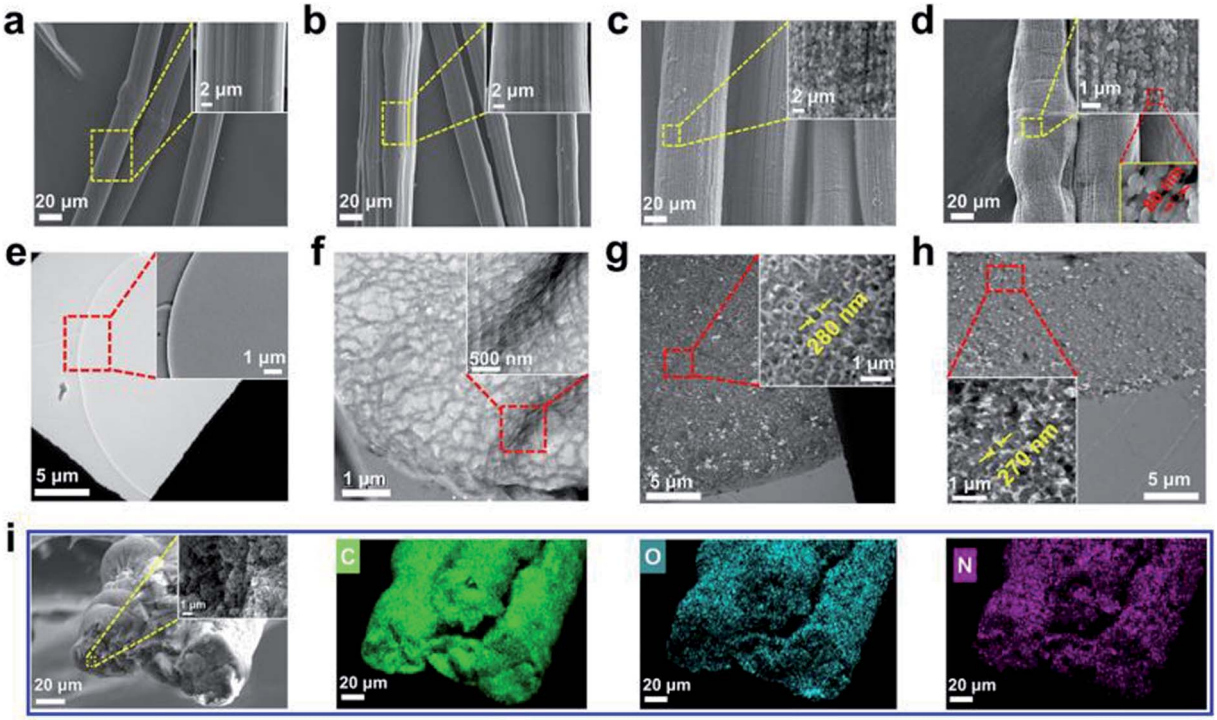

Fig. 2 Morphology characterization. SEM images of (a) UHMWPE, (b) PHEA, (c) PAN, and (d) AO-OpNpNc fibers. TEM images of (e) UHMWPE, (f) PHEA, (g) PAN, and (h) AO-OpNpNc fibers. The insets show high-magnification images. (i) EDS mapping of AO-OpNpNc fibers. SEM and TEM images of the AO-OpNpNc fiber showing the interconnected open-pore architecture, PAO nanoparticle (270 ± 2 nm), and nano-channel structure of the samples.

The EDS mapping of N and C showed that amidoxime groups were widely distributed across the entire surface and in the cross-section of the AO-OpNpNc fiber (Fig. 2i). The morphologies of the PAN and AO-OpNpNc fibers were strongly influenced by the DG of the PAN. An appropriate DG in the range of 150–400% produced optimal morphologies of the nanoparticles and nano-channels because of the self-assembly of the axial grafting chains (Fig. S5a–i and S6a–e, ESI†).

To investigate the porosity and pore structures, N_2 sorption isotherms were measured. As shown in Fig. 3a and S7a (ESI),† both the UHMWPE and PHEA fibers exhibited similar N_2 sorption behaviors, suggesting there were no porous structures. The trunk UHMWPE fibers exhibited a very low BET specific surface area of 1.7 $m^2\ g^{-1}$. The value decreased to 1.0 $m^2\ g^{-1}$ after the RIGP of poly-HEA-*co*-PAA because of the slight increase in the diameters of the PHEA fibers. After the CIGP of poly-AN-*co*-AA and ammoximation, both the PAN and AO-OpNpNc fibers exhibited similar sorption behaviors of typical "type-IV" isotherms with type H3 hysteresis loops, suggesting their interconnected open-pore architectures comprising micropores and mesopores.[46] Because of the formation of an interconnected open-pore architectures, PAN nanoparticles, and nano-channels, the BET specific surface area of the PAN fibers was dramatically increased to 6.1 $m^2\ g^{-1}$ and reached 11.1 $m^2\ g^{-1}$ after ammoximation for the AO-OpNpNc fibers (Fig. 3a inset and Fig. S7a, ESI†), which was about 6.53 times that of the trunk UHMWPE fibers, 10 times that of the hollow-gear-morphology fibers.[32] Compared with the H-ABP fibers, the specific surface area was also greatly increased as the previous supporting PP core layer was abandoned.[26] The total pore volumes of the PAN and AO-OpNpNc fibers were 0.014 and 0.033 $cm^3\ g^{-1}$, respectively, which were 1.9 and 4.5 times higher than that of the H-ABP fibers (0.0074 $cm^3\ g^{-1}$)[26] (Fig. 3a and S7b, ESI†). The interconnected open-pore architecture and high specific surface area of the AO-OpNpNc fibers provided numerous nano-channels for the continuous mass transport (Fig. 1b), thereby leading to an enhanced adsorption capacity.[47]

3.2 Crystal structure and thermal stability of AO-OpNcNp fibers

The XRD patterns of the fibers are shown in Fig. 3b. The characteristic diffraction peaks at 21.7° and 24.0° of the crystal structure of the UHMWPE were observed in the spectra of the UHMWPE, UHMWPE pre-irradiated with 40 kGy, PHEA, PAN, AO-OpNpNc, and AO-OpNpNc fibers after KOH treatment.[48] This result suggests that the crystal structures of the AO-OpNpNc fibers were maintained after chemical modification. The two main diffraction peaks (d_{110} = 4.08 Å, d_{200} = 3.68 Å) were assigned to the (110) and (200) planes of the UHMWPE (Fig. 3c).[49] No significant changes in the diffraction positions and *d*-spacing (d_{110} and d_{200}) were evident during the synthesis process, suggesting the conservation of the orthorhombic crystal arrangement of UHMWPE molecules (Fig. 3b, c, Tables S1 and S2, ESI†). Compared with the trunk UHMWPE fibers, the full width at half maximum (FWHM) of the AO-OpNpNc fibers increased by 0.26° for (110) and 0.27° for (200) (Fig. S8, ESI†),

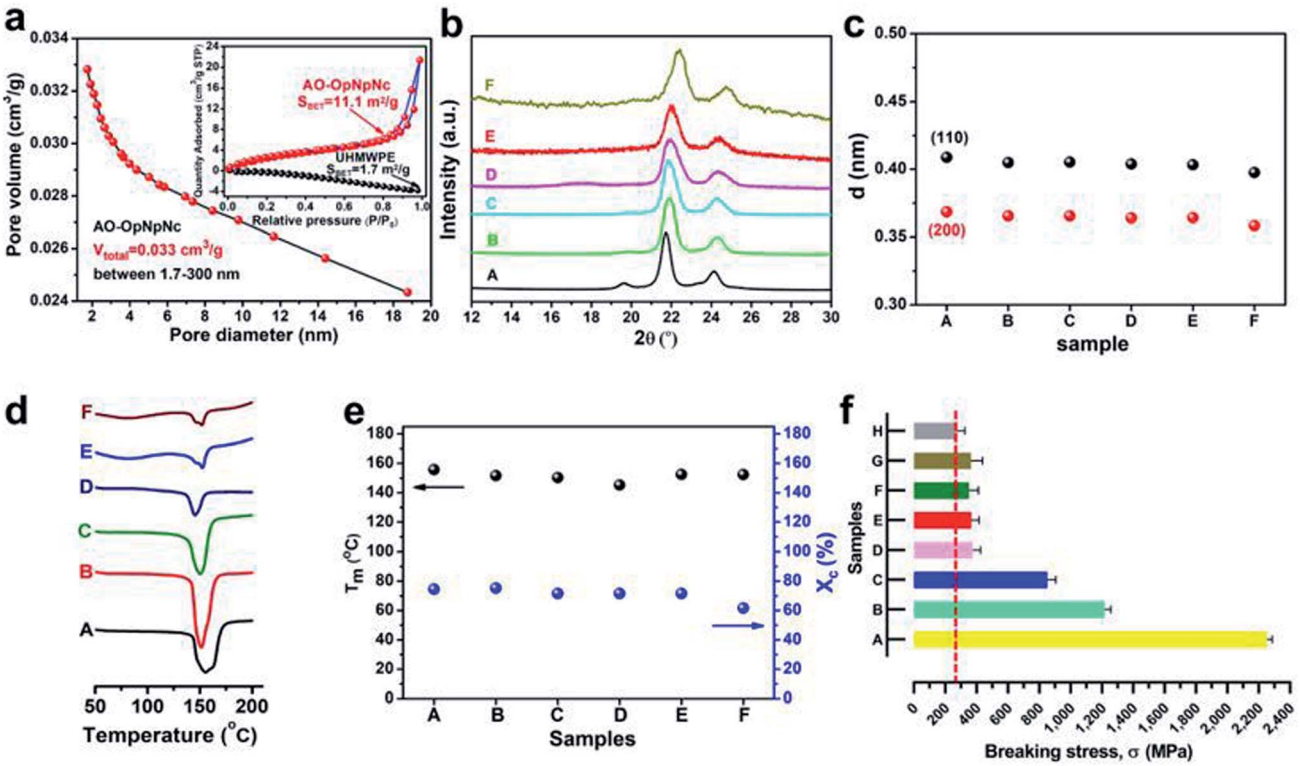

Fig. 3 Physiochemical characterization and interconnected open-pore architecture analysis. (a) Pore diameter distributions of the AO-OpNpNc fibers. Inset: N_2 sorption isotherms of the UHMWPE and AO-OpNpNc fibers. (b) XRD patterns, (c) FWHM, (d) DSC patterns, (e) T_m and X_c evolution, and (f) breaking strength of a single fiber during the preparation process of the adsorbents: (A) UHMWPE, (B) pre-irradiation of UHMWPE with 40 kGy, (C) PHEA, (D) PAN, (E) AO-OpNpNc, (F) AO-OpNpNc after KOH treatment, (G) AO-OpNpNc after KOH treatment in a wet state, and (H) AO-OpNpNc after 30 adsorption–desorption cycles.

which suggests the crystalline regularity decreased slightly. Upon irradiation, chain scission and crosslinking could simultaneously occur owing to the formation and recombination of free radicals in the amorphous region. Chain scission could improve the mobility of broken chains near the crystalline region, resulting in new small lamellae.[50] Consequently, crystalline regularity was destroyed. Additionally, the crystalline regularity could be negatively affected by grafting. The variation of the crystallinity during the synthesis process was determined by DSC (Fig. 3d). No evident changes in the melting temperature (T_m) and the degree of crystallinity (X_c) were observed during the synthesis process (Fig. 3e). The shoulder peak from the AO-OpNpNc fiber in Fig. 3d suggests a slight increase in the FWHM and a slight decrease in the crystalline regularity. The thermogravimetric analysis (TGA) and derivative thermogravimetry (DTG) curves for the UHMWPE, PHEA, PAN, and AO-OpNpNc fibers presented in Fig. S9 (ESI)† shows that the obtained fiber samples have good thermal stabilities. The trunk UHMWPE fibers showed high thermal stabilities up to 473 °C, without any residue at 500 °C (Fig. S9a, ESI†). The TGA-DTG curves (Fig. S9b, ESI†) of the PHEA fibers revealed two main decomposition processes. The first occurred in the temperature range from 301 to 430 °C, while the second one occurred from 432 to 502 °C. The weight loss was due to the complex thermal decomposition of the carboxylic groups and graft chains. For the PAN fibers (Fig. S9c, ESI†), five regions of weight loss, *i.e.*, 30.5 to 100 °C, 100 to 175 °C, 241 to 340 °C, 346 to 443 °C, and 445 to 582 °C, occurred due to dehydration, decarboxylation of AA groups, cyclization, carbonization of the PAN, and carbonization of the HEA molecular chains, respectively. The TGA-DTG curve showed that the first region, between 50 and 100 °C, corresponded to the evaporation of physisorbed water, which was due to the AO-OpNpNc fibers with an interconnected open-pore architecture and nano-channel structure as well as the good hydrophilicity. After amidoximation (Fig. S9d, ESI†), the AO-OpNpNc fibers became less thermally stable compared to the PAN fibers, and degradation began at approximately 134 °C. However, the thermal stability of the UHMWPE fibers remained unchanged after graft modification. The chemical and thermal stabilities of the main chain suggest that the AO-OpNpNc fibers are suitable for ocean environments.

The mechanical strength of a single fiber is a key factor in the field of UES, as each fiber should be able to withstand the force of the ocean current. The representative breaking strength and stress–strain curves of the fiber samples are presented in Fig. 3f and S10 (ESI),† respectively. The breaking strength of the trunk UHMWPE fiber, UHMWPE fiber after pre-irradiation with 40 kGy, PHEA fiber, PAN fiber, AO-OpNpNc fiber, and AO-OpNpNc fiber in a dry state after KOH conditioning were 2241.0, 1202.3, 837.7, 362.0, 352.3, and 334.0 MPa, respectively (Fig. 3f(A–F)).

The wet state of the AO-OpNpNc fiber after KOH conditioning exhibited a slightly higher mechanical strength of 344.8 MPa (Fig. 3f(G)). After 30 adsorption–desorption cycles, the mechanical strength was as high as 266.7 MPa (Fig. 3f(H)), which is higher than any fibrous adsorbent for UES that has been reported.

3.3 Uranium adsorption from simulated seawater

The uranium adsorption capacity and stability of the AO-OpNpNc fibers were studied in a simulated seawater system following the same procedure as in a previous study.[26,45] As the results show in Table S3 (ESI),† the adsorption capacities of uranium and the competing ions V, Fe, Co, Ni, Cu, Zn, Pb, Mg, and Ca were 15.98, 0.33, 3.12, 0.082, 0.08, 0.60, 2.64, 0.35, 10.62 and 12.45 mg-U per g-adsorbent, respectively. Impressively, the AO-OpNpNc fiber showed not only a high uranium adsorption capacity of 15.98 mg-U per g-adsorbent (Fig. 5a and Table S3, ESI†) but also a higher capacity than all the competing ions including V, Mg and Ca. A series of AO-OpNpNc fibers with different DGs and amidoxime densities were studied. The DG of poly-AN reached hundreds to one thousand, while the amidoxime density of the AO-OpNpNc fibers increased with the DG and became saturated at 8.3 mmol g^{-1} (Fig. 5b). The high amidoxime density corresponded to more active sites of the adsorbent and the uranium adsorption capacity increased with the DG and amidoxime density. The AO-OpNpNc fibers, with a DG of 307.0% and amidoxime density of 7.7 mmol g^{-1} adsorbed 100% of the uranium from solution, and a uranium adsorption capacity of 17.70 mg-U per g-adsorbent was obtained. Further increases in the DG did not provide advantages for the amidoxime density or adsorption capacity, as the sizes of the nanoparticles increased, and the nano-channel structure was blocked (Fig. S5 and S6, ESI†).

3.4 Investigation of uranyl binding interactions in the AO-OpNcNp fibers

The SEM images, EDS mapping, and TEM images of the cross-section of the uranium loading in the AO-OpNpNc fiber showed that uranium was distributed across the entire cross-section of the AO-OpNpNc fiber (Fig. 4a and b). Compared with the full scan XPS spectrum of the AO-OpNpNc fibers, two new peaks at 382.48 and 393.12 eV were found, which were special peaks of U 4f (Fig. 4c). The uranyl ion (O=U=O) is the most common form of uranium found in terrestrial and aquatic environments.[51] In the FT-IR spectra of the AO-OpNpNc fiber before and after uranium adsorption (Fig. S11, ESI†), the –N–O– redshift from 920 to 903 cm^{-1}, as well as the intensity of the peak, was enhanced, owing to the stretching frequency of the linear structure of the O=U=O and –C=N–OH binding. To gain further insight, X-ray absorption fine structure (XAFS) spectroscopy was applied to confirm the coordination environment of the uranyl in the AO-OpNpNc fibers. Analysis of the extended

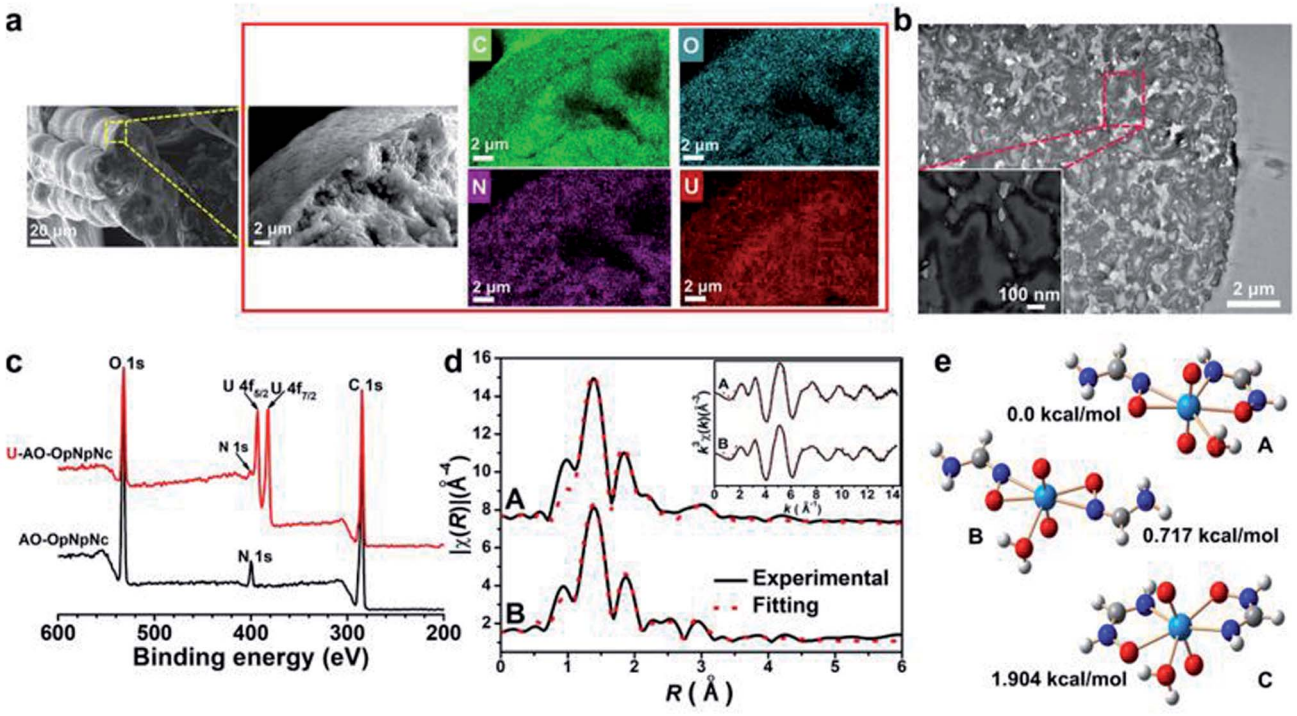

Fig. 4 Uranyl binding interactions in the AO-OpNpNc fiber. (a) EDS of the U-AO-OpNpNc fiber cross section. (b) TEM images of the U-AO-OpNpNc fiber cross section. Inset: high-magnification image. (c) XPS spectra of AO-OpNpNc and U-AO-OpNpNc fibers. (d) EXAFS data (black line) and fits (red dots) of the AO-OpNpNc fibers exposed to (A) a pure uranyl solution and (B) a uranyl tricarbonate solution. Inset: corresponding data and fit displayed in *k*-space. (e) DFT calculation of the binding enthalpies. Structures of uranyl complexes with amidoxime obtained after geometric optimization at the B3lyp/6-311G(d,p) level of theory.

Table 1 EXAFS fits for AO-OpNpNc fibers exposed to (A) uranyl ion solution and (B) uranyl tricarbonate solution[a]

Shell	R (Å)	CN	σ^2 ($\times 10^{-3}$ Å^2)	R-factor
(A) uranyl ion solution				
U–O_{ax}	1.79 ± 0.01	2[b]	2 ± 0.6	0.012
U–O	2.36 ± 0.02	3.1 ± 0.4	4 ± 2	
U–N_1	2.53 ± 0.02	2.1 ± 0.2	2 ± 1	
U–N_2	3.43 ± 0.03	2.1 ± 0.7	4 ± 3	
U–C	3.61 ± 0.04	2.1 ± 0.6	5 ± 0.3	
(B) uranyl tricarbonate solution				
U–O_{ax}	1.80 ± 0.01	2	2 ± 0.8	0.012
U–O	2.34 ± 0.02	3.1 ± 0.5	3 ± 2	
U–N_1	2.51 ± 0.03	2.1 ± 0.4	3 ± 1	
U–N_2	3.41 ± 0.04	2.1 ± 0.8	4 ± 2	
U–C	3.57 ± 0.05	2.1 ± 0.6	7 ± 4	

[a] R is the bond length. CN is coordination number. σ^2 is the mean squared relative displacement. [b] The coordination number for U–O_{ax} was held at 2 for the model.

XAFS (EXAFS) region, as displayed in Fig. 4d, S12, and S13 (ESI)† revealed that the AO-OpNpNc fibers bound to uranyl in a similar fashion in both uranyl and uranyl tricarbonate solutions. The k^3-weighted EXAFS data and their corresponding Fourier transform (FT) spectra are shown in the inset of Fig. 4d. AO-OpNpNc fibers exposed to the uranyl solution were fit by a model composed of three shells of scattering elements (Fig. 4d and Table 1). The first shell comprised two axial O atoms of the uranyl groups (O_{ax}), with their coordination numbers fixed. The second and third shells contain a variable number of O and N, each with different path lengths. The EXAFS fitting parameters are shown in Table 1. Two O_{ax} that were separated by a distance of ~1.79 Å, which is typical of uranyl compounds, were found in the two samples.[22,40] The equatorial coordination environment of the uranyl groups contained 5.2 ± 0.6 or 5.2 ± 0.9 light-scattering elements, while the third shell contained 4.2 ± 1.3 light-scattering elements of both N and C or 4.2 ± 1.4 light-scattering elements of both N and C in the uranyl or uranyl tricarbonate solutions, respectively (Table 1). The proposed interaction between the uranyl and amidoxime group, including monodentate,[52] tridentate,[53,54] η^2 binding[15,40] and chelating,[55] were reported previously. Results from the coordination numbers, bond lengths, mean squared relative displacement (σ^2), and R-factor in Table 1 are consistent with the average local coordination environment of the uranyl containing two amidoximes bound in a chelating fashion (Fig. 4d and e(A)). Results from the density functional theory (DFT) calculation showed that a five-coordinate 1 : 2 uranyl complex with mixed coordination of the two ligands was more stable than that with the η^2 binding model[22] (Fig. 4e(A) and Table S4, ESI†). Beyond simply identifying the uranyl bonding environment, there was no evidence to suggest that binding of uranyl by cyclic imide dioxime occurred, which is consistent with the results of a previous study.[22] The structures of open chain amidoxime and cyclic imide dioxime affect the binding of uranium and vanadium. V binds preferentially with cyclic imide dioxime groups and does not bind well with open chain amidoxime.[10] The results above indicated that the open-chain amidoxime was more favorable than cyclic imide dioxime for binding uranium, which was also found in a previous study.[10] The ^{13}C CP/MAS spectra of the AO-OpNpNc fiber a before and after KOH treatment are illustrated in Fig. S14 (ESI).† The signals at 149.8 ppm and a small shoulder centered at 155.6 ppm are ascribed to cyclic imide dioxime and open chain amidoxime of AO-OpNpNc fibers, respectively.[26] The ^{13}C CP/MAS spectra of AO-OpNpNc fibers after KOH treatment shown a slightly stronger signal at 149.8 ppm (Fig. S14, trace B, ESI†) and a relatively stronger shoulder centered at 155.6 ppm.[26] The results indicated that the AO-OpNpNc fibers after KOH treatment may have contained less cyclic imide dioxime and more open chain amidoxime than the AO-OpNpNc fibers, which may be one of the main reasons the average adsorption capacity of uranium was higher than that of vanadium.

3.5 Recyclability of AO-OpNpNc fibers

The service life and stability of the AO-OpNpNc fibers were studied by adsorption–desorption experiments for 30 cycles in a simulated seawater system.[26] During the 30 adsorption–desorption cycles, the adsorption capacity of uranium remained in the range of 16.33–13.28 mg-U per g-adsorbent, and there was no tendency to decrease (Fig. 5a), revealing that the AO-OpNpNc fiber could be reused for at least 30 cycles. The total amount of uranium in the AO-OpNpNc fibers during 30 cycles reached 447.6 mg-U per g-adsorbent (Fig. S15, ESI†). Uranium could be eluted with 0.1 M HCl efficiently. After 30 cycles of accumulation, very small amounts of U (0.12 mg-U per g-adsorbent, 0.049%) were found in the adsorbents (Fig. S16a, b, and Table S5, ESI†). Compared with uranium, vanadium and iron were more difficult to be eluted;[15] 30.22% of V and 4.17% of Fe were measured in the AO-OpNpNc fibers after 30 cycles of accumulation (Fig. S16b and Table S5, ESI†). The morphologies of the AO-OpNpNc fibers after 30 adsorption–desorption cycles show that the ordered morphology with PAO nanoparticles and the nano-channels structure was well maintained in highly saline water and resisted elution and regeneration (Fig. S16c, ESI†). Fig. S17† shows the uranium capacities of the AO-OpNpNc fibers as functions of the contact time. The AO-OpNpNc fibers reached adsorption equilibrium after 30 h with a uranium adsorption capacity of 19.2 mg-U per g-adsorbent. A high specific surface area, high total pore volume, high mechanical strength, and high structural stability enabled the AO-OpNpNc fiber uranium adsorption capacity to be 15.98 mg-U per g-adsorbent in this simulated seawater system for a service life of 30 adsorption–desorption cycles, which is a new record in the field of UES.

3.6 Uranium extraction from natural seawater

The adsorption behavior of the AO-OpNpNc fibers with natural seawater was studied, and the results are shown in Fig. 5c and S18 (ESI).† During the batch adsorption process, the uranium adsorption ratio increased rapidly, and 28.45% uranium could be adsorbed from the natural seawater after 10 d. The adsorption ratio slowed to 47.0% until 42 d, and the capacity of

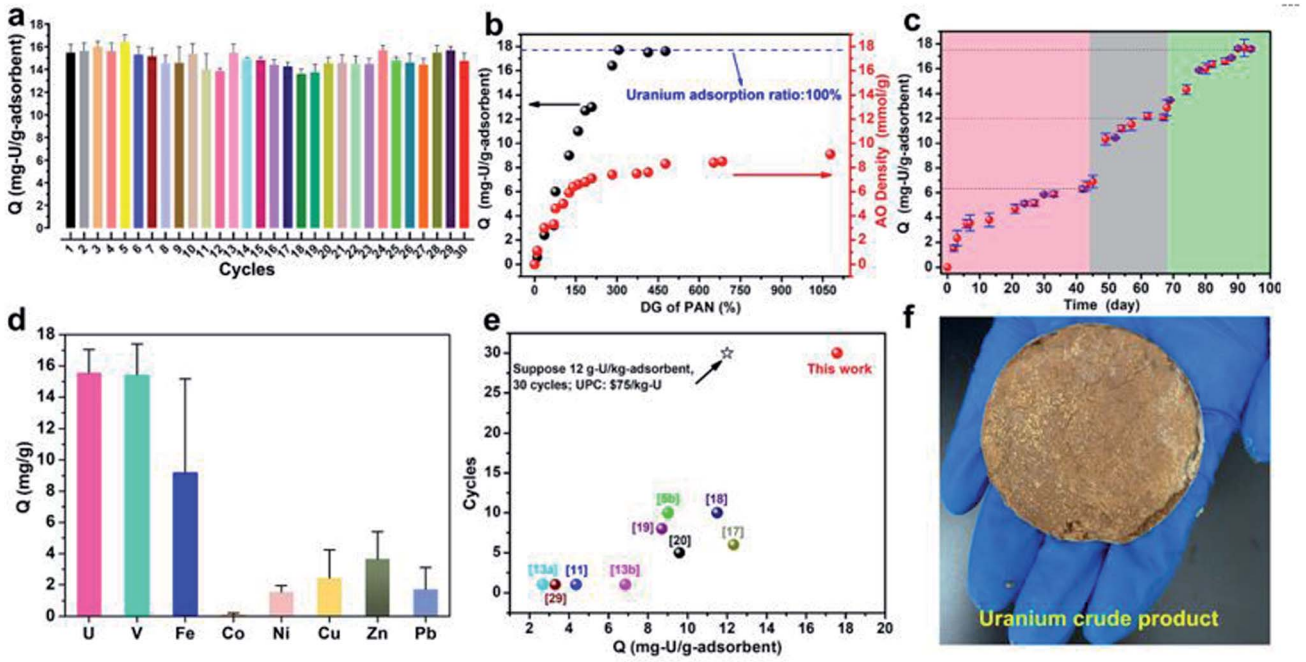

Fig. 5 Evaluation of uranium adsorption capacity and service life. (a) Uranium adsorption capacity during 30 adsorption–desorption cycles of AO-OpNpNc fibers with an initial uranium concentration of 330 ppb and coexisting ions. (b) AO density, uranium adsorption capacity, and uranium adsorption ratio of AO-OpNpNc fibers with different DGs. (c) Uranium adsorption capacities of AO-OpNpNc fibers after different contact periods with natural seawater. (d) Capacities of uranium and co-existing ions after 90 d of adsorption in natural seawater. (e) Comparation of uranium adsorption capacity on various representative adsorbents. (f) Recovery of 5.6 g of uranium in its crude form from the ocean.

uranium reached 6.30 mg per g-adsorbent, which is higher than the H-ABP fiber[26] and hollow gear fibers[29,32] reported previously. The uranium capacity increased to 11.57 mg-U per g-adsorbent after 56 d of adsorption in natural seawater. In the batch adsorption system, the adsorption capacity did not continuously increase after 42 d because the concentration of uranium in the system was low. Once fresh seawater was charged, the adsorption capacity continuously increased, and the growth tendency was similar to that during the first adsorption round. Another 30 d of adsorption with fresh seawater resulted in a uranium capacity of 12.09 mg g^{-1}-adsorbent, which was much higher than that of the H-ABP fibers.[26] The third round of fresh seawater was charged, and after 30 d, the capacity of uranium reached 17.57 mg g^{-1}-adsorbent, which is a new record in the field of UES. After three rounds of adsorption, AO-OpNpNc fibers were eluted, and the capacity of uranium and other competing ions in the materials were shown in Table S6 (samples 1–3) (ESI).† The AO-OpNpNc fiber showed not only a high uranium capacity of 17.57 mg g^{-1}-adsorbent but also a higher capacity than all competing ions, which agreed with the results in the simulated seawater system. Adsorption was also studied with flow-through tests in the coastal marine areas. The color of the AO-OpNpNc fibers changed from light yellow to dark brown after 90 d of adsorption in natural seawater (Fig. S19, ESI†). Numerous marine microorganisms adhered to the surfaces of the fibers, and even after careful washing, there were still numerous contaminants (Fig. S20, ESI†). The results of the adsorption capacities of all metal ions are shown in Table S6 (samples A–C) (ESI)† and Fig. 5d. Because of the contamination of marine microorganisms, the uranium adsorption capacity was 15.42 mg-U per g-adsorbent, slightly lower than that obtained in the laboratory, which indicated that antimicrobial contamination is important in the process of UES. Nonetheless, after 90 d of adsorption, the average adsorption capacity of uranium reached 15.42 mg-U per g-adsorbent, which was higher than that of the competing ions V, Fe, Co, Ni, Cu, Pb, and Zn. To the best of our knowledge, this is both the longest service life and the highest uranium adsorption capacity of adsorbents in natural seawater (Fig. 5e). Encouragingly, a total of 5.6 g uranium in its crude product was extracted from seawater by the porous fibrous adsorbent in 90 d at the Tropical Marine Biological Research Station in Hainan, Chinese Academy of Sciences, Sanya, China (Fig. 5f).

3.7 Economic evaluation and outlook

Researchers have systematically estimated the UPC for braided adsorbent-based extraction systems.[30,56] A supposed 12 mg-U per g-adsorbent adsorption capacity and 30 uses corresponded to a production cost of $75 per kg of uranium,[30] which is comparable to the uranium spot price ($55–87 per kg of uranium, 2015–2020).[31] The UPC analysis is divided into three steps: adsorbent production, braid deployment and retrieval, and uranium elution and purification. Each step is associated with four parts: capital, materials, operating costs, and elution and purification, in which the materials represent 20% of the total UPC.[30] According to adsorbent production cost evaluated by Japanese researchers, the trunk material only accounts for 8.3% of the adsorbent production cost.[30,56] The spot price of the

UHMWPE fibers is 10 times that of common PE fibers, which means that if UHMWPE is used as the trunk fibers instead of PE fibers, the adsorbent production cost will increase by 75%. The adsorbent production cost can also be evaluated according to the spot price in the Chinese market (fiber modification reaction: liquor ratio 1 : 25, DG = 200%): for the spot prices of PE fibers, UHMWPE fibers, and chemical reagents, if PE is replaced with UHMWPE fibers, the adsorbent production cost will increase by 38% (Fig. S21, ESI†). Accordingly, a 38–75% increase in the adsorbent material production cost results in a UPC increase of 8–15%, as the adsorbent material production cost only accounts for 20% of the total UPC.[30] The UPC could only increase from \$75 per kg of uranium to \$80.70–86.25 per kg of uranium using this material, which finally meets the criteria for the economic evaluation of UES. Furthermore, it is similar to the uranium spot price of \$86.68 per kg of uranium and lower than the prices of all currently available adsorbents, which is strongly competitive with land-based uranium mining (Fig. S21, ESI†). The cost for UES is close to the uranium price in the spot uranium market, suggesting that the AO-OpNpNc fibers could be used for economical UES.

4. Conclusions

In summary, we developed an interconnected open-pore architecture fibrous adsorbent with PAO nanoparticles and a nano-channel structure for highly efficient and economical UES. The top-down design using macromolecules in the form of a continuous fibrous material provides a new approach for the fabrication of interconnected open-pore architectures. Attributed to the well-designed structure, the AO-OpNpNc fiber showed an ultrahigh uranium adsorption capacity, an excellent mechanical strength, and an ultra-long service life. The chemical chelation mode between the PAO and uranyl was verified by EXAFS and DFT computational studies. The high uranium adsorption capacity of 17.57 mg-U per g-adsorbent in natural seawater with a service life of 30 adsorption–desorption cycles resulted in a UPC of \$80.70–86.25 per kg of uranium, which is a significant milestone in the process of UES. The exceptional durability, high efficiency, and economic AO-OpNpNc fiber is a promising adsorbent to eventually provide commercially attractive nuclear fuel derived from the oceans—the largest source of uranium on earth.

Conflicts of interest

There are no conflicts to declare.

Acknowledgements

This research was supported by the National Natural Science Foundation of China (grant numbers U1732151, 21676291, U1832124, U1832152) and the Strategic Priority Research Program of the Chinese Academy of Sciences (XDA02030000). The authors thank Tropical Marine Biological Research Station in Hainan, South China Sea Institute of Oceanology, CAS and Guangdong Zhong Ke Bao Biotechnology Co., Ltd providing the workplace for uranium extraction from natural seawater.

Notes and references

1 Word Nuclear Association, https://www.world-nuclear.org/information-library/country-profiles/countries-a-f/china-nuclear-power.aspx., 2020.
2 S. Chu and A. Majumdar, *Nature*, 2012, **488**, 294–303.
3 C. Tsouris, *Nat. Energy*, 2017, **2**, 17022.
4 D. S. Sholl and R. P. J. N. Lively, *Nature*, 2016, **532**, 435–437.
5 H. Lindner and E. Schneider, *Energy Econ.*, 2015, **49**, 9–22.
6 S. Zhao, Y. Yuan, Q. Yu, B. Niu, J. Liao, Z. Guo and N. Wang, *Angew. Chem., Int. Ed.*, 2019, **58**, 14979–14985.
7 C. Liu, P.-C. Hsu, J. Xie, J. Zhao, T. Wu, H. Wang, W. Liu, J. Zhang, S. Chu and Y. Cui, *Nat. Energy*, 2017, **2**, 17007.
8 Y. Yuan, Y. Yang, X. Ma, Q. Meng, L. Wang, S. Zhao and G. Zhu, *Adv. Mater.*, 2018, **30**, 1706507.
9 C. W. Abney, R. T. Mayes, T. Saito and S. Dai, *Chem. Rev.*, 2017, **117**, 13935–14013.
10 A. S. Ivanov, C. J. Leggett, B. F. Parker, Z. Zhang, J. Arnold, S. Dai, C. W. Abney, V. S. Bryantsev and L. Rao, *Nat. Commun.*, 2017, **8**, 1560.
11 S. Das, S. Brown, R. T. Mayes, C. J. Janke, C. Tsouris, L. J. Kuo, G. Gill and S. Dai, *Chem. Eng. J.*, 2016, **298**, 125–135.
12 T. Saito, S. Brown, S. Chatterjee, J. Kim, C. Tsouris, R. T. Mayes, L.-J. Kuo, G. Gill, Y. Oyola, C. J. Janke and S. Dai, *J. Mater. Chem. A*, 2014, **2**, 14674–14681.
13 J. Wen, Q. Li, H. Li, M. Chen, S. Hu and H. Cheng, *Ind. Eng. Chem. Res.*, 2018, **57**, 1826–1833.
14 Z. Zhuang, H. Chen, Z. Lin and Z. Dang, *Environ. Sci.: Nano*, 2016, **3**, 1254–1258.
15 Q. Sun, B. Aguila, J. Perman, A. S. Ivanov, V. S. Bryantsev, L. D. Earl, C. W. Abney, L. Wojtas and S. Ma, *Nat. Commun.*, 2018, **9**, 1644.
16 Q. Sun, B. Aguila, L. D. Earl, C. W. Abney, L. Wojtas, P. K. Thallapally and S. Ma, *Adv. Mater.*, 2018, **30**, 1705479.
17 Y. Li, X. Guo, X. Li, M. Zhang, Z. Jia, Y. Deng, Y. Tian, S. Li and L. Ma, *Angew. Chem., Int. Ed.*, 2020, **59**, 4168–4175.
18 W.-R. Cui, C.-R. Zhang, W. Jiang, F.-F. Li, R.-P. Liang, J. Liu and J.-D. Qiu, *Nat. Commun.*, 2020, **11**, 436.
19 L. Chen, Z. Bai, L. Zhu, L. Zhang, Y. Cai, Y. Li, W. Liu, Y. Wang, L. Chen, J. Diwu, J. Wang, Z. Chai and S. Wang, *ACS Appl. Mater. Interfaces*, 2017, **9**, 32446–32451.
20 Y. Yuan, S. Feng, L. Feng, Q. Yu, T. Liu and N. Wang, *Angew. Chem., Int. Ed.*, 2020, **132**, 4292–4298.
21 Y. Ying, A. M. Pourrahimi, Z. Sofer, S. Matějková and M. Pumera, *ACS Nano*, 2019, **13**, 11477–11487.
22 C. W. Abney, R. T. Mayes, M. Piechowicz, Z. Lin, V. S. Bryantsev, G. M. Veith, S. Dai and W. Lin, *Energy Environ. Sci.*, 2016, **9**, 448–453.
23 C. Ma, J. Gao, D. Wang, Y. Yuan, J. Wen, B. Yan, S. Zhao, X. Zhao, Y. Sun, X. Wang and N. Wang, *Adv. Sci.*, 2019, **6**, 1900085.
24 J. Kim, C. Tsouris, R. T. Mayes, Y. Oyola, T. Saito, C. J. Janke, S. Dai, E. Schneider and D. Sachde, *Sep. Sci. Technol.*, 2013, **48**, 367–387.

25 Y. Yuan, Q. Yu, J. Wen, C. Li, Z. Guo, X. Wang and N. Wang, *Angew. Chem., Int. Ed.*, 2019, **58**, 11785–11790.
26 X. Xu, H. Zhang, J. Ao, L. Xu, X. Liu, X. Guo, J. Li, L. Zhang, Q. Li, X. Zhao, B. Ye, D. Wang, F. Shen and H. Ma, *Energy Environ. Sci.*, 2019, **12**, 1979–1988.
27 D. Wang, J. Song, J. Wen, Y. Yuan, Z. Liu, S. Lin, H. Wang, H. Wang, S. Zhao, X. Zhao, M. Fang, M. Lei, B. Li, N. Wang, X. Wang and H. Wu, *Adv. Energy Mater.*, 2018, **8**, 1802607.
28 Y. Yuan, S. Zhao, J. Wen, D. Wang, X. Guo, L. Xu, X. Wang and N. Wang, *Adv. Funct. Mater.*, 2019, **29**, 1805380.
29 J. Kim, C. Tsouris, Y. Oyola, C. J. Janke, R. T. Mayes, S. Dai, G. Gill, L.-J. Kuo, J. Wood, K.-Y. Choe, E. Schneider and H. Lindner, *Ind. Eng. Chem. Res.*, 2014, **53**, 6076–6083.
30 Technology and applied R&D Needs for nuclear fuel resources, 2010, *Nuclear Fuel Resources Workshop*, Norwood, Massachusetts, USA, October 13–15, 2010.
31 Uranium-price, https://www.cameco.com/invest/markets/uraniumprice, 2020.
32 Y. Oyola, C. J. Janke and S. Dai, *Ind. Eng. Chem. Res.*, 2016, **55**, 4149–4160.
33 J. Zhao, W. Han, H. Chen, M. Tu, R. Zeng, Y. Shi, Z. Cha and C. Zhou, *Carbohydr. Polym.*, 2011, **83**, 1541–1546.
34 E. Oral, A. S. Malhi and O. K. Muratoglu, *Biomaterials*, 2006, **27**, 917–925.
35 B. Ravel and M. J. Newville, *J. Synchrotron Radiat.*, 2005, **12**, 537–541.
36 M. J. Newville, *J. Synchrotron Radiat.*, 2001, **8**, 322–324.
37 A. Lavrentyev, I. Y. Nikiforov, V. Dubeiko, B. Gabrelian and J. J. Rehr, *J. Synchrotron Radiat.*, 2001, **8**, 288–290.
38 M. J. Frisch, G. W. Trucks, H. B. Schlegel, G. E. Scuseria, M. A. Robb and J. R. Cheeseman, *et al.*, *Gaussian 09*, Gaussian, Inc., Wallingford, CT, 2009.
39 C. Lee, W. Yang and R. G. Parr, *Phys. Rev. B: Condens. Matter Mater. Phys.*, 1988, **37**, 785–789.
40 S. Vukovic, L. A. Watson, S. O. Kang, R. Custelcean and B. P. Hay, *Inorg. Chem.*, 2012, **51**, 3855–3859.
41 W. Küchle, M. Dolg, H. Stoll and H. Preuss, *J. Chem. Phys.*, 1994, **100**, 7535–7542.
42 X. Cao and M. Dolg, *J. Mol. Struct.: THEOCHEM*, 2004, **673**, 203–209.
43 C. Z. Wang, J. H. Lan, Q. Y. Wu, Q. Luo, Y. L. Zhao, X. K. Wang, Z. F. Chai and W. Q. Shi, *Inorg. Chem.*, 2014, **53**, 9466–9476.
44 J. Kim, Y. Oyola, C. Tsouris, C. R. Hexel, R. T. Mayes, C. J. Janke and S. Dai, *Ind. Eng. Chem. Res.*, 2013, **52**, 9433–9440.
45 J. Hu, H. Ma, Z. Xing, X. Liu, L. Xu, R. Li, C. Lin, M. Wang, J. Li and G. Wu, *Ind. Eng. Chem. Res.*, 2016, **55**, 4118–4124.
46 Z. Xu, Y. Zhang, P. Li and C. Gao, *ACS Nano*, 2012, **6**, 7103–7113.
47 M.-H. Sun, S.-Z. Huang, L.-H. Chen, Y. Li, X.-Y. Yang, Z.-Y. Yuan and B.-L. Su, *Chem. Soc. Rev.*, 2016, **45**, 3479–3563.
48 F. Lv, X. Chen, C. Wan, F. Su, Y. Ji, Y. Lin, X. Li and L. Li, *Macromolecules*, 2017, **50**, 6385–6395.
49 L. Balzano, B. Coussens, T. Engels, F. Oosterlinck, M. Vlasblom, H. van der Werff and D. Lellinger, *Macromolecules*, 2019, **52**, 5207–5216.
50 P. Hyun Kang and Y. Chang Nho, *Radiat. Phys. Chem.*, 2001, **60**, 79–87.
51 M. Keener, C. Hunt, T. G. Carroll, V. Kampel, R. Dobrovetsky, T. W. Hayton and G. Menard, *Nature*, 2020, **577**, 652–655.
52 E. G. Witte, K. S. Schwochau, G. Henkel and B. Krebs, *Inorg. Chim. Acta*, 1984, **94**, 323–331.
53 F. Endrizzi, A. Melchior, M. Tolazzi and L. Rao, *Dalton Trans.*, 2015, **44**, 13835–13844.
54 G. Tian, S. J. Teat and L. Rao, *Dalton Trans.*, 2013, **42**, 5690–5696.
55 S. P. Kelley, P. S. Barber, P. H. K. Mullins and R. D. Rogers, *Chem. Commun.*, 2014, **50**, 12504–12507.
56 M. Tamada, in *International seminar on nuclear war and planetary emergencies—42nd Session*, World Scientific, 2010, pp. 243–252.

